LUND UNIVERSITY

Thermal analysis of a high-power glow discharge in flowing atmospheric air by combining Rayleigh scattering thermometry and numerical simulation

Kong, Chengdong; Li, Zhongshan; Aldén, Marcus; Ehn, Andreas

PAPER • OPEN ACCESS

Thermal analysis of a high-power glow discharge in flowing atmospheric air by combining Rayleigh scattering thermometry and numerical simulation
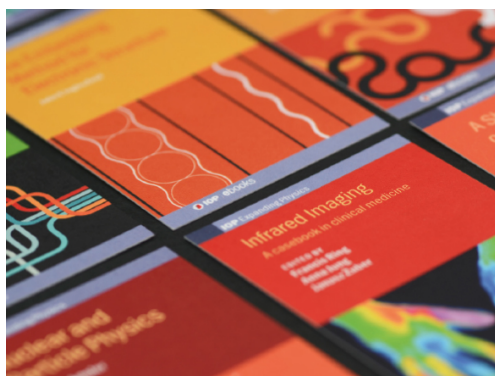
View the article online for updates and enhancements.

Thermal analysis of a high-power glow discharge in flowing atmospheric air by combining Rayleigh scattering thermometry and numerical simulation

Chengdong Kong[1]**, Zhongshan Li, Marcus Aldén and Andreas Ehn**

Division of Combustion Physics, Lund University, PO Box 118, S-221 00 Lund, Sweden

E-mail: kongcd1987@gmail.com

CrossMark

Abstract

The thermal state of a glow discharge with intermediate current in flowing atmospheric air is investigated by a combination of Rayleigh scattering thermometry imaging and numerical simulation. Results from the simulation indicate that during the initial breakdown the local translational temperature can reach a huge value (e.g. 6000 K) but decreases quickly due to strong heat transfer to the surrounding cold air. In the gliding stage, the translational temperature of plasma is balanced by the input power density and the heat dissipation rate. As the gas flow rate is increased, the translational temperature in the glow plasma column diminishes. The flow affects the thermal state of plasma from two aspects. First, it promotes elongation of the plasma column to decrease the input power density. Second, the flow enhances local heat dissipation. As a result, the translational temperature is lowered due to flow. Using a two-temperature model, which considers the translational temperature, the vibrational temperature and their transitions, the non-thermal state of plasma is further analyzed. The gas flow is found to reduce the translational temperature and the vibrational–translational relaxation rate, and thus prevent thermalization of the plasma column.

Keywords: high-power glow discharge, thermal state, Rayleigh scattering thermometry, flow effect

(Some figures may appear in colour only in the online journal)

1. Introduction

Plasma discharge at atmospheric pressure has attracted increasing interest in recent decades owing to the low operating cost and valuable applications in combustion enhancement [1–3], surface treatment [4], welding [5], nanoparticle synthesis [6], decontamination [7], etc. Typical plasma sources operable at atmospheric pressure include arc discharge, dielectric barrier discharge (DBD), corona discharge, glow discharge and nanosecond pulsed discharge. These plasma sources always have specific applications, depending on their thermal states, which can be quantified by the electron (T_e), translational (T_g), rotational (T_{rot}), and vibrational (T_{vib}) temperatures and qualitatively characterized by thermal equilibrium or non-equilibrium. Generally, an arc discharge, which has temperatures exceeding 6000 K and T_e, T_{vib}, T_{rot} and T_g close to each other is thermal, while DBD, corona and glow discharges are always in non-thermal equilibrium with a temperature ordering of $T_e > T_{vib} > T_{rot} \sim T_g$ [8–10]. For a more quantitative characterization of the thermal states of various plasma sources, quantitative measurements of T_e, T_{vib}, T_{rot} and T_g are necessary. T_e can be measured by the Thomson scattering technique [11, 12] or estimated from the reduced

---

[1] Author to whom any correspondence should be addressed.

J. Phys. D: Appl. Phys. **53** (2020) 085502

C Kong *et al*

electric field strength (E/N) [8]. T_{vib} and T_{rot} can be derived from optical emission spectroscopy (OES) [8, 13, 14] or the Raman scattering technique [15–17]. It should be stressed that the so-called vibrational or rotational temperature is not accurately defined in a realistic non-equilibrium plasma. Different species in the plasma can have discrepant vibrational or rotational temperatures. For instance, the rotational temperature of the excited OH(A) species is larger than that obtained from N_2(C–B) emission [14]. T_g can be calculated by Rayleigh scattering thermometry (RST) [8, 18, 19] or estimated from the rotational temperature [20]. Typical ranges for these different temperatures were measured for a gliding arc discharge by Zhu *et al* [8], listing electron, vibrational, rotational and translational temperatures of 8700 K, 5900 K, 4300 K and 1100 K, respectively.

Recently, an atmospheric pressure glow discharge has been stabilized at an intermediate current range (50–200 mA) [21], and its translational temperature spans a large range from 2000 K to 5000 K. An intermediate-current glow discharge is always contracted (referred to as arcing) but still has different T_e and T_g. It can be regarded as a hybrid discharge lying between diffusive glow discharge and the thermal arc [21]. Driven by gas flow, this type of glow discharge can also move, forming a so-called gliding glow discharge [22]. A glow discharge with intermediate current has a high power density and could have numerous potential applications in industry. However, because of its non-stationary and contracted properties, the thermal state of an intermediate-current glow discharge in flow is difficult to investigate and not well characterized.

To characterize the thermal states of a glow discharge, OES has been widely used for measurements of T_g, T_{rot} and T_{vib} [8, 13, 14, 20], but this technique detects the line-integrated spontaneous emissions from the luminous zone and only focuses on the central plasma column without much consideration of the surroundings. Actually, the surrounding translational temperature distribution and flow field are highly interactive with the central plasma column. Two-dimensional (2D) RST seems to be the most-promising technique for detecting the translational temperature profile of the plasma core and its surroundings.

For a glow discharge at atmospheric pressure, the flow disturbance needs to be considered. But with the addition of a flow disturbance, the explanation and description of the thermal properties of plasma become more complicated. Due to the influence of the flow, the electrical discharge characteristics and the temperature profiles vary over time. Absence of information about the local flow field hinders further exploration of the thermal states of plasma in flow.

This article aims to investigate the thermal state of an intermediate-current contracted glow plasma discharge under flow disturbance and provide a detailed explanation of the energy transport surrounding the plasma column through a combination of the RST technique and a numerical method. RST with a pulsed laser was used to visualize the translational temperature profiles around the non-stationary plasma column. Numerical simulations by combining the fluid dynamics and heat transfer process were performed to clarify the impacts of flow on the heat transfer. The numerical simulations can qualitatively predict the whole thermal history of the discharge from breakdown to plasma propagation, and thus shed light on the heating process during discharge. Based on the experimental and numerical results, the thermal properties of a plasma column under different flow conditions and current–voltage inputs are discussed.

2. Methodology

2.1. Experimental setup

Figure 1 shows a schematic of the experimental setup. A hybrid McKenna-type burner, featuring a central tube (ID 2 mm) to provide a jet flow and a 60 mm diameter brass porous plug to produce a laminar co-flow, is used to manipulate the flow field. The co-flow, which has a flow rate of 160 l min^{-1} at room temperature to get a mean velocity of 0.94 m s^{-1}, is employed here to shield the particles from the open air. Hence, the strong Mie scattering from dust particles can be reduced to a minimum during the Rayleigh scattering measurement. The flow rate of the central jet is varied from 0 l min^{-1} to 20 l min^{-1} to produce a laminar or a turbulent jet flow in the central zone. Two tungsten needles, which are used as electrodes for the discharge, are located approximately 2 cm above the exit of the central tube. One electrode is connected to an AC power supply (Generator 9030 E, SOFTAL Electronic GmbH) whereas the other is grounded. In order to control the duration of the discharge, the power supply is set to the burst mode [23], which means that the AC high voltage trains from the power supply are loaded for a certain time period (t_{on}) and off for another time period (t_{off}). t_{on} and t_{off} can be independently adjusted by the pulse generator (BNC 575, Berkeley Nucleonics Corp.). A current monitor (Pearson Electronics) and voltage probe (Tektronix P6015A) were employed to measure the waveforms of the current and voltage simultaneously. The typical current and voltage waveforms are presented in the inset of figure 1. This indicates that as the high voltage reaches the breakdown threshold the discharge is initialized, along with current spikes. After the breakdown stage, the discharge transits to a glow discharge with relatively low current and voltage. The glow regime is confirmed by estimation of the cathode fall (about 460 V) and the low current peak value of around 400 mA. During this stage, the plasma column moves downstream, driven by flow, and elongates. Meanwhile, the value of the peak current changes slightly with elongation of the plasma column at the glow discharge stage.

The planar Rayleigh scattering measurements were conducted using the second harmonic of a Brilliant B laser (Quantel). A half-wave plate was inserted to change the polarization of the laser beam for the maximum Rayleigh scattering signal. An intensified charge-coupled device (ICCD) camera (PI Max II, Princeton Instruments) equipped with a visible Nikon lens (*f*/1.4, 50 mm) was used to acquire the Rayleigh signals. For synchronization, the BNC pulse generator was used to externally trigger the Brilliant B laser and the power generator while the ICCD camera was externally triggered by the output signal from the laser. The current and voltage
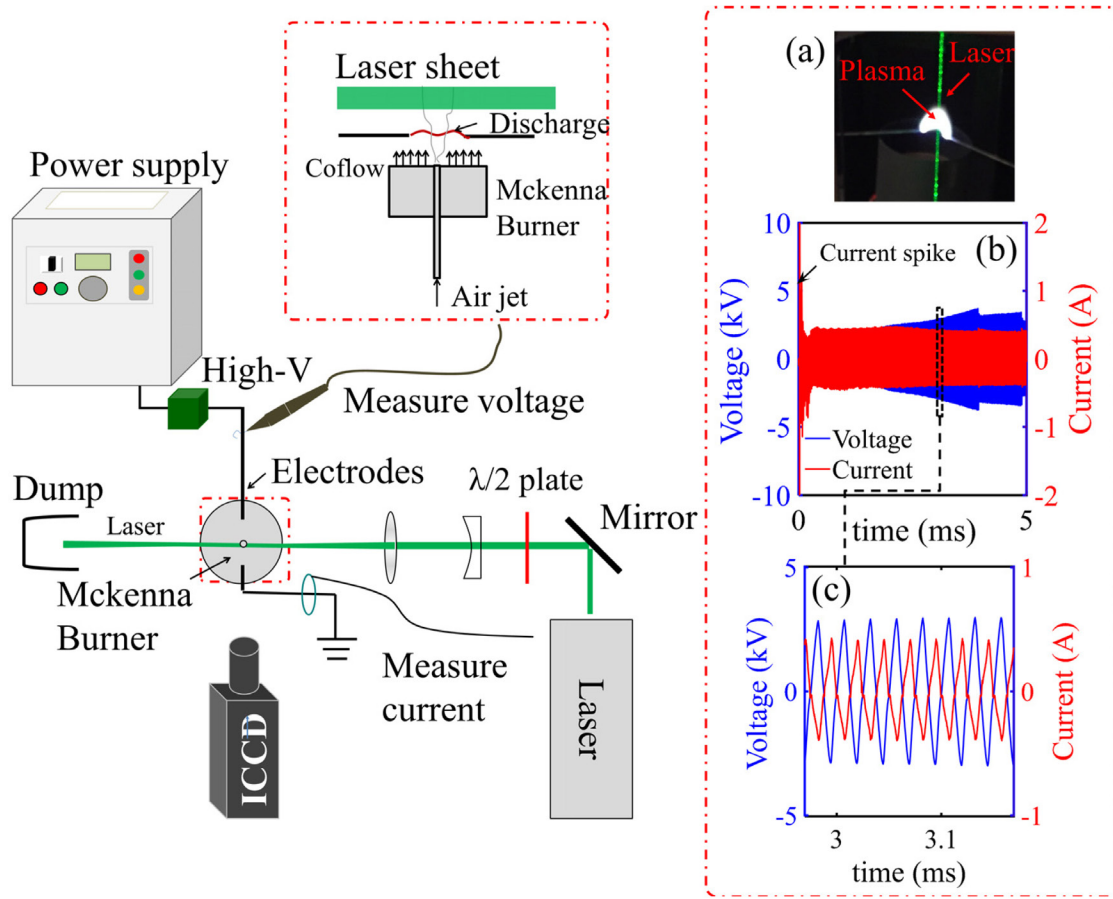
Figure 1. Schematic of the experimental setup. The inset on the right-hand side shows the image of the plasma and laser sheet (a) and the current/voltage waveforms (b). Part (c) shows the zoomed current and voltage waveforms. The phase of the current is inversely plotted to distinguish it from the voltage.

signals together with the ICCD gate signal were simultaneously recorded using a four-channel oscilloscope (PicoScope 4424, PS) at a sampling rate of 2 GHz.

2.2. Principle of Rayleigh scattering thermometry [8, 24]

The intensity of the Rayleigh scattering signal (I_R) from a gas mixture is given as

$$I_R = \text{Const} \times I_0 \times \left(\sum_i N_i \sigma_i \right), \tag{1}$$

where Const is a constant determined by the collection efficiency, the probe volume and so on, I_0 is the incident laser intensity, and N_i and σ_i are the number density and the Rayleigh cross-section of individual species i in the probed gas mixture, respectively. The number density of species is dependent on pressure, temperature and mole fraction, which has been formulated by the ideal gas law:

$$N_i = P C_i / k_B T_g, \tag{2}$$

where P is the pressure, C_i is the mole fraction of species i, k_B is the Boltzmann constant and T_g is the translational temperature of the gas.

Substituting equation (2) into equation (1) yields equation (3):

$$I_R = \text{Const} \times I_0 \times \left(\frac{P}{k_B T_g} \right) \bar{\sigma} \tag{3}$$

where $\bar{\sigma}$ is the averaged Rayleigh cross-section of the probed gas mixture. Equation (3) indicates that the Rayleigh scattering intensity is inversely proportional to the gas temperature, provided that the gas composition and the Rayleigh cross-sections are constant.

To calculate the absolute gas temperature around the plasma column, the Rayleigh scattering signal is compared with a reference target, which is usually the open air at room temperature (RT), as indicated by equation (4)

$$\frac{I_{R,a}}{I_{R,RT}} = \left[\frac{I_{0,a} \bar{\sigma}_a}{T_{g,a}} \right] \bigg/ \left[\frac{I_{0,RT} \bar{\sigma}_{RT}}{T_{g,RT}} \right], \tag{4}$$

where the subscripts a and RT denote the plasma and room temperature, respectively. Rearranging equation (4) yields a formula for the gas temperature around the plasma column ($T_{g,a}$) (see equation (5))

$$T_{g,a} = T_{g,RT} \times (I_{R,RT}/I_{R,a}) \times [I_{0,a} \bar{\sigma}_a / I_{0,RT} \bar{\sigma}_{RT}]. \tag{5}$$

In the experiment, 100 single-shot images of the scattering signal from air at room temperature are collected to calculate the averaged $I_{R,RT}$ in the post-processing, while $I_{R,a}$ is derived from a single-shot image. This means that $I_{0,RT}$ is an averaged value, the same as $I_{R,RT}$, while $I_{0,a}$ is a single-shot value. Since

J. Phys. D: Appl. Phys. **53** (2020) 085502

C Kong *et al*

the laser pulse is not perfectly repeatable but varies slightly from pulse to pulse, the ratio of $I_{0,RT}$ and $I_{0,a}$ is not exactly equal to 1, which can lead to uncertainties.

2.3. Uncertainty analysis of Rayleigh scattering thermometry

Based on equation (5), the overall uncertainties of temperature from RST can be formulized as equation (6):

$$\frac{\Delta T_{g,a}}{T_{g,a}} = \frac{\Delta T_{g,RT}}{T_{g,RT}} + \frac{\Delta (I_{R,RT})}{I_{R,RT}} - \frac{\Delta (I_{R,a})}{I_{R,a}} + \frac{\Delta (I_{0,a}/I_{0,RT})}{I_{0,a}/I_{0,RT}} + \frac{\Delta (\bar{\sigma}_a/\bar{\sigma}_{RT})}{\bar{\sigma}_a/\bar{\sigma}_{RT}},\quad(6)$$

where the first term on the right-hand side represents the uncertainty of room temperature, the second and third terms represent the uncertainties from the Rayleigh scattering signals of air and plasma, the fourth term represents the uncertainty from the shot-to-shot laser jittering and the fifth term represents the uncertainty of the cross-sections of gaseous species.

In the laboratory the uncertainty of room temperature is small and can be neglected. The uncertainties of $I_{R,RT}$ and $I_{R,a}$ are mainly from the stray light. So I_R can be divided into two parts, the Rayleigh scattering signal of probed gas molecules ($I_{R,sig}$) and the signal due to the stray light ($I_{R,str}$), as represented by equation (7):

$$I_R = I_{R,sig} + I_{R,str}.\quad(7)$$

An estimation of this uncertainty is performed as follows. The stray light intensity is assumed to be linearly dependent on the laser intensity, which is clearly proportional to Rayleigh scattering signal at room temperature, i.e.

$$I_{R,str} = Const_1 \times I_{R,RT,sig}.\quad(8)$$

Hence, the second and third terms on the right-hand side of equation (6) can be reframed as:

$$\frac{\Delta (I_{R,RT})}{I_{R,RT}} = Const_1 \times I_{R,RT,sig}/I_{R,RT}\quad(9)$$

$$\frac{\Delta (I_{R,a})}{I_{R,a}} = Const_1 \times I_{R,RT,sig}/I_{R,a}.\quad(10)$$

Assuming $Const_1$ be equal to 1%, the uncertainties due to the stray light in the air and plasma are respectively estimated to be 1% and $T_{g,RT}/T_{g,a} \times 1\%$. This means that the impact of stray light is amplified at higher temperatures. The uncertainty of laser sheet signal, together with the pixel uncertainty, is estimated to be 4.5% by post-processing 100 single-shot laser sheet images without plasma using Matlab software.

The Rayleigh cross-section of gaseous species, depending on the chemical compositions in the plasma column, is uncertain. Some numerical simulations found that the oxygen molecules could be largely dissociated into atomic oxygen in the plasma [25, 26]. This greatly influences the averaged Rayleigh scattering signal, according to the cross-sections of different species listed in table 1 [27–29]. In this article the plasma discharge is driven by an AC power supply. According to the previous investigation [30], the chemical compositions inside the plasma column can be approximated using a chemical equilibrium model which assumes the chemical composition is close to an equilibrium state corresponding to

Table 1. Cross-sections of different species for 532 nm light.

Species	Cross-section (10^{-27} cm^2)
Ar	4.45
N_2	5.1
CO	6.19
O_2	4.74
N	3.526
O	1.204
H	0.86
NO	5.2

an effective temperature (~4500 K). Using the CEA program [31], the chemical compositions in the plasma column is thus estimated. The corrected average cross-section ($\bar{\sigma}$) is 20% lower than that of pure air. This means that the temperature derived from RST can be overestimated by nearly 20% when the change of chemical composition is not considered.

In short the uncertainty of temperature can be estimated by equation (11)

$$\frac{\Delta T_{g,a}}{T_{g,a}} = \frac{T_{g,a}}{T_{g,RT}} \times Const_1 - 20\% \pm 4.5\%.\quad(11)$$

It is worth noting that uncertainty about the cross-section occurs in the plasma region, where the temperature is the highest. Therefore, the measured peak temperature has large potential error bars; however, away from the plasma column the measured temperature is more accurate. The impact of stray light ($Const_1$) is difficult to estimate but its impact diminishes with the decrease in temperature. So the temperature outside the plasma core has smaller uncertainties than that in the plasma core.

2.4. Numerical model of the heat transfer process during discharge

The governing equations of heat transfer during discharge can be expressed by the Navier–Stokes equation and the energy conservation equation, given by equations (12) and (13)

$$\rho \frac{\partial u_g}{\partial t} + \rho u_g \cdot \nabla u_g = \nabla \cdot \left(-p_g I + \mu_g \left(\nabla u_g + \nabla u_g^T\right)\right)\quad(12)$$

$$\rho c_p \frac{\partial T_g}{\partial t} + \rho c_p u_g \cdot \nabla T_g - \nabla \cdot k \nabla T_g = Q_s,\quad(13)$$

where ρ is the gas density, u_g is the gas velocity, p_g is the gas pressure, μ_g is the gas viscosity, I is the unit matrix (the superscript T represents the tensor transpose operation), c_p is the heat capacity at constant gas pressure, k is the gas thermal conductivity and Q_s is the heating power density.

The whole discharge process is basically divided into two sub-processes, i.e. breakdown and plasma propagation. The breakdown process occurs quite fast and violently, so the gas must be treated as a compressible flow, while the plasma propagation process is gentle, and thus the gas flow can be approximated as an incompressible flow. Because of this difference, the breakdown process and the propagation process are simulated separately. Here Comsol commercial software
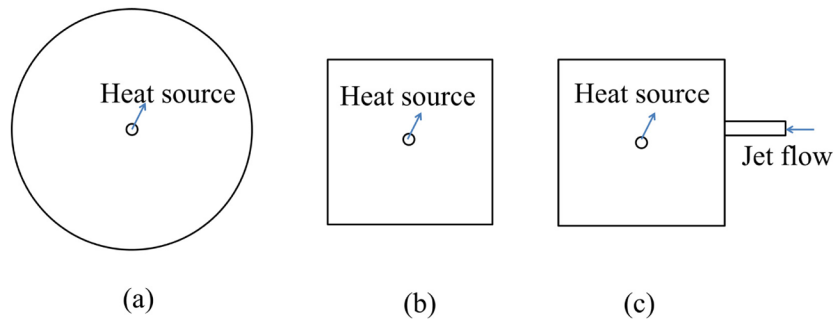
Figure 2. Simulation geometries for different simulation cases: (a) breakdown, (b) stationary flow, (c) jet flow.
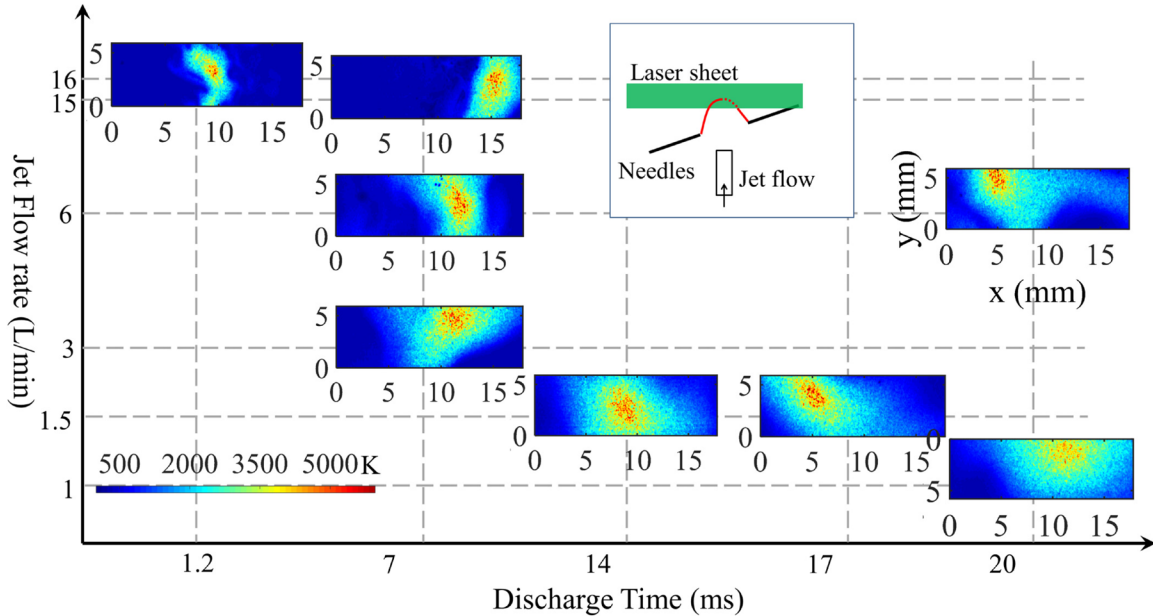

Figure 3. Translational temperature distributions around the plasma column with respect to the jet flow rate and discharge duration time.

is chosen to perform the simulation since it provides appropriate modules to simulate the breakdown and plasma propagation processes. The breakdown process is modeled using the high Mach number flow module while the plasma propagation process is simulated using the common heat transfer module and the incompressible flow module. In this work, a two-dimensional (2D) simulation on the cross-section of the plasma column is performed. Different simulation geometries are chosen for the given simulation cases, as shown in figure 2. For the breakdown case, a relatively large round-shaped volume is used. The breakdown is assumed to occur in the center, where a pulsed heat source with a Gaussian profile is imposed to model the heating process during breakdown. The initial temperature is 300 K and the initial flow is static. The radius of the simulation volume is 0.1 m, large enough to allow the pressure wave produced by breakdown to propagate away from the initial source. A square-shaped volume with a size of 67.2 mm × 67.2 mm × 1m is adopted for the simulation of propagation process. The plasma column is confined to a small volume so the input energy is represented by a heat source with a radius of 0.5 mm. The temperature profile obtained from the breakdown simulation at 200 μs is used as the initial temperature profile for the propagation simulation

and the initial flow is still assumed static. The boundary conditions for the heat transfer and the flow processes are thermal insulation and constant pressure, respectively. In order to study the effect of flow on the temperature profiles and heat dissipation, a jet flow is further introduced, as shown in figure 2(c).

3. Results and discussion

3.1. Temperature profile around the plasma channel under different flow conditions

In the experiment, a laser sheet forms across the moving plasma column to detect the translational temperature profiles on the cross-section of the plasma, as shown in the inset of figure 3. The jet flow rate and the discharge time together with the distance between the laser sheet and the electrodes are varied to study their influences on the temperature profiles around the plasma column. Figure 3 shows the temperature distributions with respect to the jet flow rate and the discharge time and figure 4 demonstrates the corresponding peak translational temperatures as a function of the flow rate and discharge time. The peak temperature in figure 4 is an averaged value in a volume with a radius of 0.5 mm without any temperature
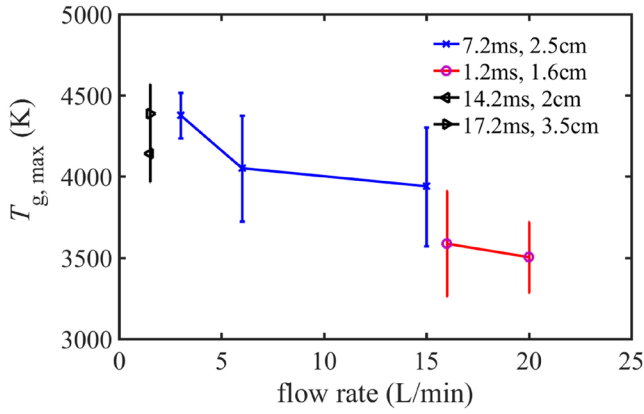
Figure 4. Peak temperature measured by the Rayleigh scattering technique with respect to the jet flow rate.

correction. It basically decreases from 4400 K to 3500 K with the increase in jet flow rate. The peak temperature can also increase with discharge duration when the flow rate is quite slow. As analyzed in section 2.3, the value of peak temperature is quite uncertain and some corrections need to be made. When the decomposition of oxygen molecules is considered but the impact of stray light is ignored, the peak temperature is estimated to vary from 3500 K to 2800 K. When the stray light is further considered by assuming $Const_1 = 1\%$, the peak temperature can be around 4000–3200 K according to equation (11).

As shown in figure 3, the temperature profiles change a lot due to the jet flow and the discharge duration. When the jet flow rate is 0 l min^{-1}, the flow field is laminar and the temperature profile is not stretched by convection, the heat transfer is mainly governed by heat conduction, resulting in a roughly round-shaped profile. From the T_g profile, the temperature gradient can be estimated to be ~730 kK m^{-1}. Using a conductivity of 0.1 W m^{-1} K^{-1} and a radius of 5 mm, the heat dissipation rate is 2.3 kW per meter of plasma column. As the jet flow rate increases, the temperature profiles become unstable and stretched or twisted by the flow, resulting in the higher local temperature gradient. Furthermore, the size of the hot region decreases as the jet flow rate increases. The size of the hot region around the plasma column is dependent on the discharge duration time because the heat from the plasma column needs time to spread out. For the case controlled by heat conduction, the size can be estimated by the thermal diffusion length, which is given by equation (14)

$$L_{dif} \approx \sqrt{D_{dif} t_{dif}}, \tag{14}$$

where D_{dif} is the thermal diffusivity and t_{dif} is heat conduction time. When the convection is included, the hot region shrinks, mainly due to the improved heat dissipation to reduce the temperature.

3.2. Numerical analysis of the translational temperature profile

The time-resolved translational temperature profiles during the breakdown process as well as the plasma gliding stage in the flow could not be acquired by experiment. Nevertheless,
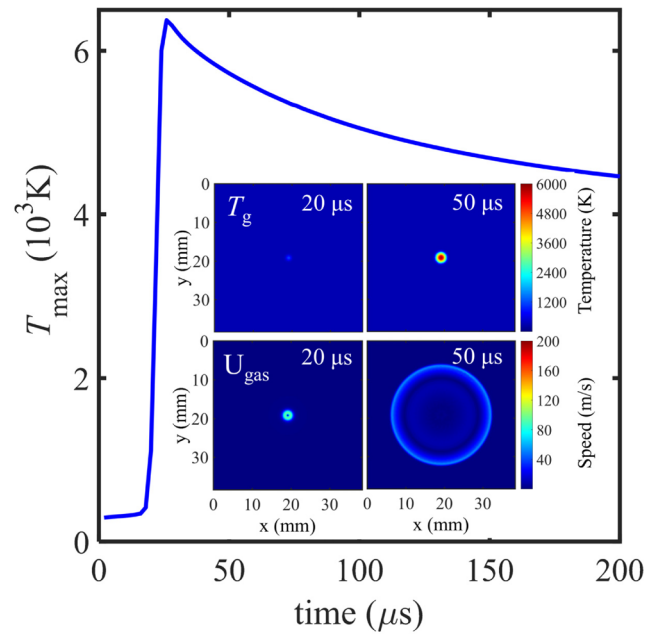
Figure 5. Simulated peak temperature variations during the breakdown process, together with the temperature and velocity profiles sampled at 20 μs and 50 μs.

through numerical simulation, the breakdown process and the impacts of flow can both be analyzed.

3.2.1. Discharge-induced heating process in a static flow condition. The heating process during breakdown is approximated to that caused by a pulsed heating source. The duration and total energy input of the heating pulse determine the propagation speed of the pressure wave and the peak temperature. By shortening the pulse duration, the pressure wave propagates faster since more energy can be converted to kinetic energy of the gas. An increment in pulsed energy can result in a higher temperature. For the current simulation case, the pulsed heat source is assumed to follow a spatio-temporal Gaussian profile, expressed as equation (15)

$$Q_s = 3 \times 10^6 \exp\left[-\frac{r^2}{2r_{arc}^2}\right] / 2\pi r_{arc}^2 \times \exp\left[-\frac{(t - t_0)^2}{2\tau^2}\right] / \sqrt{2\pi}, \tag{15}$$

where r_{arc} is the effective size of the plasma column, equal to 0.5 mm, and τ is the standard deviation of the temporal Gaussian profile, equal to 1.7 μs. The simulated peak temperature variation and the velocity profiles are demonstrated in figure 5. This indicates that the maximum temperature can reach 6373 K during the breakdown process, and after the pulse heating the temperature drops to 4500 K within 150 μs due to the rapid heat dissipation. The initial propagation speed of the pressure wave can be 200 m s^{-1} because of the fast gas heating, but drops quickly along the radial direction. The disturbance on the local flow field from breakdown almost disappears after 50 μs in the discharge zone.

After breakdown, the heating process is simulated using an incompressible flow module. The temperature variation is governed by the input power of the heating source (Q_s). Provided that the power of the heat source is constant and
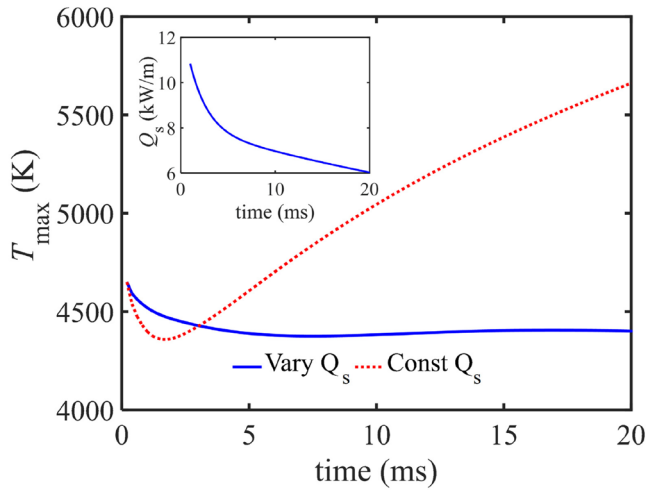
Figure 6. Variation of the peak temperature of the plasma column over time when the input heat power is constant and varying. Inset: the varying heat power.

Figure 7. (a) Temperature profiles measured by Rayleigh scattering at a jet flow rate of $0 \, \text{l min}^{-1}$. (b) Simulated temperature profiles in a static flow.

large, the peak temperature in the plasma drops first but starts to increase l.6 ms later, as shown in figure 6. The initial heating process during breakdown is localized in the plasma column since the breakdown occurs much faster than the heat transfer process. It results in a huge temperature gradient around the plasma column just after breakdown. Later the temperature decreases because of rapid heat conduction driven by the large temperature gradient. With the thermal energy spreading out, the temperature gradient decreases and meanwhile the rate of heat conduction declines. The peak temperature starts to increase when the input heat power is larger than that dissipated by heat conduction. In order to control the peak temperature, a heat source with decreasing power is needed. Figure 6 also shows the peak temperature over time when the heating power follows the curve in the inset. The peak temperature can stop increasing provided that the heating power decreases properly. In the experiment, when the jet flow rate is small the peak temperature could increase with discharge duration time. If the flow rate is high enough, the plasma column can elongate fast with the flow, so the power per meter of plasma column decreases with the flow and thus the plasma can be maintained in a glow state instead of thermalization.

The simulated temperature profile is compared with the experiment, as illustrated in figure 7. Since the temperature in the plasma core is so high that the error bar is large, it is not appropriate to compare the peak temperature directly. Instead the temperature profile in the outer layer is more relevant for comparison. The simulation indicates that the temperature profile is determined by the size of heat source and the diffusion length when heat conduction is dominant. Assuming a thermal diffusivity of $5 \times 10^{-4} \, \text{m}^2 \, \text{s}^{-1}$ and a time span of 20 ms, the diffusion length according to equation (14) is around 3 mm. In this simulation, the radius of the heat source is set to 0.5 mm to provide good fitting of the temperature profile.

3.2.2. Effect of flow on the temperature profile. A jet flow is introduced near the plasma column to study the effect of a free shear layer on the temperature profile, as shown in
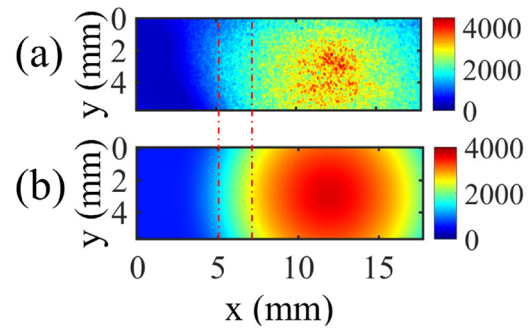
figure 8. Due to heat convection, the peak temperature drops with increase in flow rate while the temperature profiles are stretched.

Here, to simplify the analysis, a hot volume around the plasma column is defined using the contour line of temperature (e.g. 2000 K). Then the rate of heat transfer across the boundary of this hot volume can be estimated as:

$$Q_{\text{dissi}} = k \times \delta T / \delta l \times A, \tag{16}$$

where $\delta T / \delta l$ is the average temperature gradient along the contour line and A is the length of the contour line from the 2D viewpoint or the boundary area of the hot volume from the 3D viewpoint. When a cold gas jet impinges on this hot volume, its geometry is modified while a shear layer forms to increase the temperature gradient. Because of the increased temperature gradient and the boundary area, the peak temperature decreases.

The temperature gradient is known to be correlated with the local velocity gradient due to the similarity between the thermal shear layer and the momentum shear layer. For instance, the peak temperature gradient is plotted as a function of the local velocity gradient for different heating times, as shown in figure 9. With a fixed heating time, the temperature gradient increases with the velocity gradient. For a given velocity gradient, the temperature gradient can change in the opposite manner to the heating time. When the velocity gradient is smaller than $5 \, \text{s}^{-1}$, the thermal diffusion is more dominant than convection. The initial temperature gradient is large because of the fast heating during breakdown. Afterwards the temperature gradient drops due to heat conduction. However, when the velocity gradient is larger than $10 \, \text{s}^{-1}$, the temperature gradient is mainly governed by the local velocity gradient, i.e. it is controlled by convection. The temperature gradient builds up with the heating time since the surrounding cold flow becomes closer to the hot volume over time.

Because of the correlation between the temperature gradient and the velocity gradient, the temperature profile can be used to study the velocity field qualitatively. An important concept related to the velocity field around the plasma column is the so-called slip velocity, which has been proposed for a long time in the study of gliding arc discharges [32]. Theoretically, the slip velocity (U_{slip}) can be evaluated from the mean velocity gradient and the distance to plasma column (l_{slip}), given by:

J. Phys. D: Appl. Phys. **53** (2020) 085502

C Kong *et al*
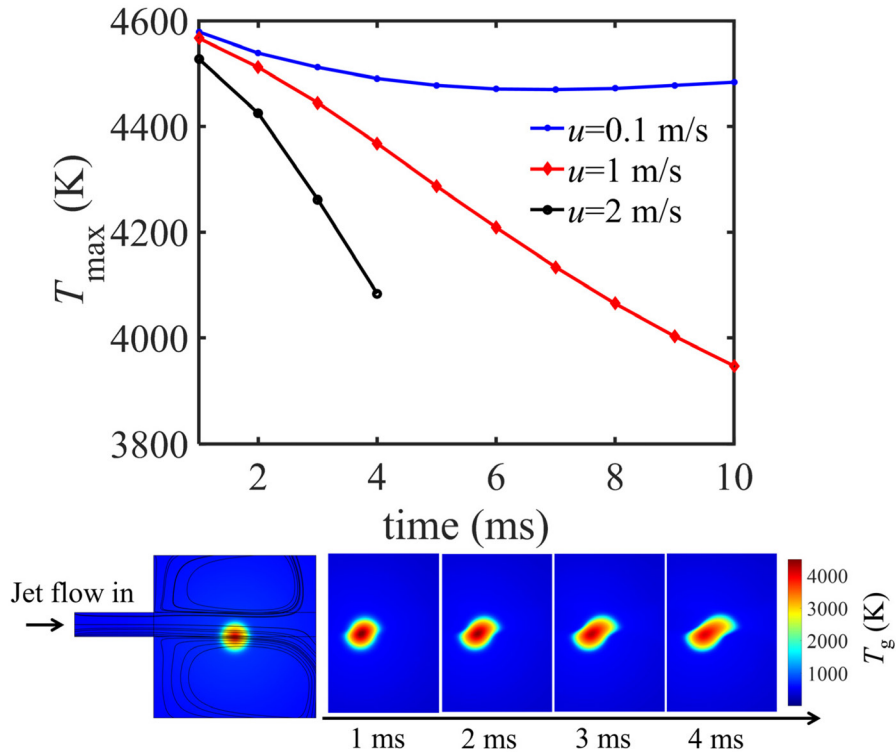
Figure 8. Simulated peak temperature variations over time for a jet flow rate of 0.1, 1 and 2 m s^{-1}, together with snapshots of temperature profiles at a jet flow rate of 2 m s^{-1}.
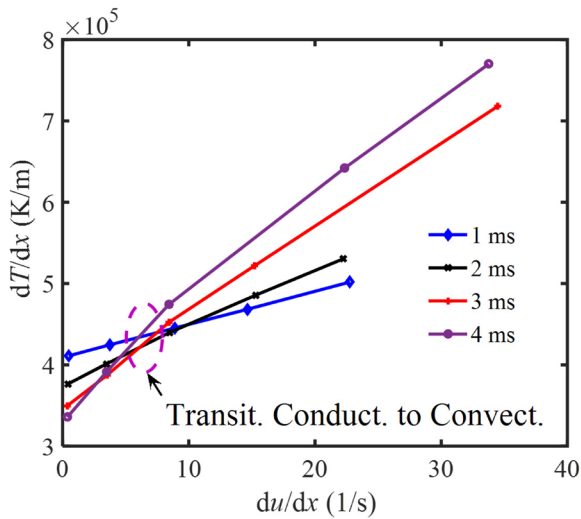
Figure 9. Peak temperature gradient as a function of the local velocity gradient for different heating times.

$$u_{slip} = \overline{\frac{\partial u}{\partial x}} \times l_{slip}. \quad (17)$$

According to figure 9, a velocity gradient of $30\,\text{s}^{-1}$ results in a remarkable increment in the temperature gradient. Assuming a distance to the plasma column of 5 mm, a slip velocity of 0.15 m s^{-1} should be distinguished in the temperature profile. Using this method, the temperature profiles under different flow rate conditions (see figure 3) can be interpreted. When the jet flow rate is 0 1 min^{-1}, the temperature profile is consistent with that simulated in a static flow. This means that

no slip velocity exists when the discharge occurs in a laminar flow without a steep velocity gradient. However, as a jet flow is present, the T_g profile is modified. The temperature gradient becomes inhomogeneous so that in some region the temperature gradient can be much larger than that in static flow, indicating a large velocity gradient. This infers that the discharge column generated in this work cannot stimulate the slip velocity automatically in a flow without an initial velocity gradient.

3.3. Analysis of the thermal state of a plasma column in air

The basic energy branching and transfer pathways in an air plasma discharge are presented as follows [33]. The input electrical energy is first absorbed by the electrons and later used to excite species, mainly the vibrational levels of nitrogen molecules in the air. Finally, the vibrationally excited nitrogen molecules transfer their energy to heat through vibrational–translational (V–T) relaxation. Under low-temperature conditions, the V–T transition process is slow and thus the vibrational temperature can be higher than the translational temperature of the molecules. To quantitatively analyze the difference between translational and vibrational temperatures in the plasma column, a two-temperature energy balance model, which was applied in [34], is introduced. Briefly, the translational temperature and the vibrational temperature of nitrogen are separately defined to describe the translational and vibrational thermal states of plasma. Using the axisymmetric approximation along the plasma column, the energy conservation equations of the translational and vibrational temperatures can be expressed by equations (18) and (19):
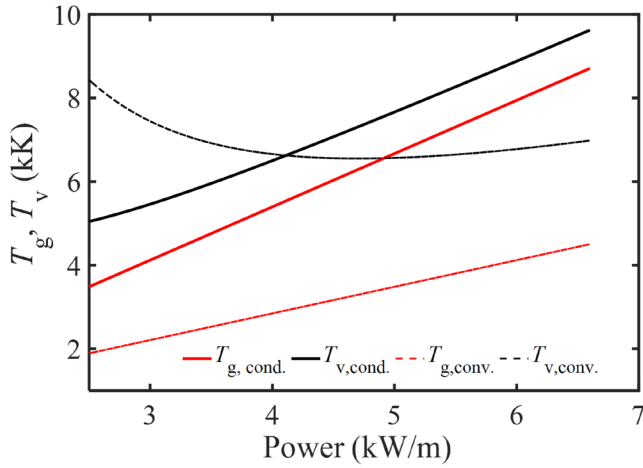
Figure 10. T_g and T_v as a function of input power per length of plasma column.

$$\frac{\rho c_p dT_g}{dt} - \frac{1}{r} \times \frac{d}{dr}\left[rk\frac{dT_g}{dr}\right] = Q_{VT} \tag{18}$$

$$\frac{n_{N_2} d\varepsilon_V}{dt} - \frac{1}{r} \times \frac{d}{dr}\left[rn_{N_2}D_{N_2}\frac{d\varepsilon_V}{dr}\right] = J \times E - Q_{VT}, \tag{19}$$

where r is the radius in the radial direction of the plasma column, ε_V is the mean vibrational energy of nitrogen molecules, n_{N_2} is the number density of nitrogen molecules, D_{N_2} is the diffusion coefficient of nitrogen molecules, J is the electrical current density, E is the electrical field strength in the plasma column and Q_{VT} is the V–T relaxation rate of N$_2$, which can be expressed through the term below:

$$Q_{VT} = \frac{n_{N_2}\left[\varepsilon_V - \varepsilon_V\left(T_g\right)\right]}{\tau_{VT}} \tag{20}$$

where τ_{VT} is the relaxation time. This describes the relaxation timescale of the vibrational energy of vibrationally excited nitrogen molecules into the translational energy of air molecules and can be expressed as [35]

$$\tau_{VT} = 6.5 \times 10^{-4}\exp\left(137/T_g^{1/3}\right)/P\,[\mathrm{Pa}]. \tag{21}$$

$\varepsilon_v(T_g)$ is the equilibrium mean vibration energy at the gas temperature, given by

$$\varepsilon_V\left(T_g\right) = E_{N_2}/\left[\exp\left(\frac{E_{N_2}}{T_g}\right) - 1\right], \tag{22}$$

where E_{N_2} is the vibrational excitation level of the nitrogen molecule (0.29 eV).

In a steady-state condition, equations (18) and (19) can be reduced to

$$-\frac{1}{r}\frac{d}{dr}\left[rk\frac{dT_g}{dr}\right] = Q_{VT} \tag{23}$$

$$-\frac{1}{r}\frac{d}{dr}\left[rn_{N_2}D_{N_2}\frac{d\varepsilon_V}{dr}\right] = J \times E - Q_{VT}. \tag{24}$$

Since the V–T transition process is much faster than the mass diffusion [36], the diffusion term on the left-hand side of equation (24) can be neglected, yielding

$$J \times E \approx Q_{VT} = \frac{n_{N_2}\left(\varepsilon_V\left(T_V\right) - \varepsilon_V\left(T_g\right)\right)}{\tau_{VT}} = -\frac{1}{r}\frac{d}{dr}\left[rk\frac{dT_g}{dr}\right]. \tag{25}$$

Equation (25) indicates that the difference between T_v and T_g is dependent on the input electrical power density, the heat dissipation rate and the V–T relaxation time. A larger input power density and a longer V–T relaxation time can give rise to a bigger difference between T_v and T_g. However, the input power density and the V–T relaxation time are always correlated through T_g in practical cases. Integration of equation (25) around the plasma column yields

$$J \times E \times \pi r_{\mathrm{arc}}^2 = -k\frac{dT_g}{dr} \times 2\pi r_{\mathrm{arc}}. \tag{26}$$

The temperature gradient is linearly approximated with equation (27)

$$\frac{dT_g}{dr} \approx -\left(T_{g,\,\mathrm{arc}} - T_{g,\mathrm{sub}}\right)/\delta r, \tag{27}$$

where $T_{g,\mathrm{arc}}$ is the temperature in the center of the plasma, $T_{g,\mathrm{sub}}$ is the temperature of the surrounding cold gas and δr represents the distance from $T_{g,\mathrm{arc}}$ to $T_{g,\mathrm{sub}}$. We assume that δr is equal to r_{arc}. $T_{g,\mathrm{arc}}$ can be derived from equations (26) and (27), given by equation (28)

$$T_{g,\mathrm{arc}} = \frac{J \times E \times \pi r_{\mathrm{arc}}^2}{2\pi k} + T_{g,\mathrm{sub}}. \tag{28}$$

This means that $T_{g,\mathrm{arc}}$ increases linearly with the input power. Combining equations (21), (22), (25) and (27), T_g and T_v in the plasma column can be estimated with the knowledge of input power and the radius of the plasma column. Figure 10 shows T_g and T_v as functions of input power per length of plasma column. It is found that a lower power results in a lower gas temperature but a larger difference between T_g and T_v. This is mainly due to the large relaxation time at low temperature. Under high-power conditions the discrepancy between T_g and T_v becomes smaller but still exists due to the energy flux from vibrational states to heat. It should also be noted that at extremely high temperature the energy conversion mechanisms could be changed, and thus the proposed two-temperature model may fail to predict the temperature difference.

Since the heat dissipation rate can be enhanced by the flow convection, the heat dissipation rate is artificially increased twice to see its impact on T_g and T_v, as shown in figure 10. It is seen that the increment of heat dissipation reduces T_g and increases T_v. So the flow convections around the plasma column can assist in sustaining the plasma in a non-thermal state as the power increases. According to this steady-state analysis, we can understand that the thermalization of the plasma column is dependent on the input power and the heat dissipation. Reducing the input power and introducing turbulent convection are ways to sustain a non-thermal plasma. In

J. Phys. D: Appl. Phys. **53** (2020) 085502

C Kong *et al*

practice, the plasma column is always fluctuating and far from the steady state. Hence, the plasma column could be easier to maintain in a non-thermal state.

4. Conclusions

Using a combination of Rayleigh scattering thermometry and numerical simulation, the thermal state of a high-power glow-type plasma column in flowing air is investigated. The numerical simulation indicates that during the initial breakdown a huge temperature increase occurs in a localized spot but its temperature drops rapidly due to the large temperature gradient between the surrounding cold gas. In the gliding glow stage, the translational temperature profiles and the peak translational temperature changes with the flow conditions. In laminar and slow flow, the T_g profile can be almost circular and well simulated by the conductive heat transfer model. The peak temperature increases with time as the input power is higher than the dissipated power. When a jet flow is introduced, the T_g profile becomes more dynamic and changes over time. Flow-induced elongation, stretching and twisting of the plasma column can reduce the local input power density. Furthermore, flow convection increases the temperature gradient to enhance the heat dissipation around the plasma column. In the end, the peak translational temperature and the hot volume around the plasma are reduced.

A two-temperature model, which combines the translational temperature and the vibrational temperature, is further applied to analyze the non-thermal state of a plasma. It indicates that the plasma becomes more thermal when the translational temperature is high and the V–T relaxation time is short. Turbulent flow can improve the heat dissipation to reduce T_g and the V–T relaxation rate for a given input power density, and thus delay or prevent the thermalization of plasma column. Therefore, introducing turbulent flow is an important method for sustaining and even manipulating the thermal state of an intermediate-current plasma.

In brief, the current work presents detailed knowledge of the energy transfer and balance in an intermediate-current glow discharge, especially under the impact of flow disturbance. It provides a method to analyze the thermal state of a high-power glow discharge, which is of interest for practical applications, and confirms that the introduction of jet flow around the plasma column is an efficient way to manipulate the thermal states.

Acknowledgment

ORCID iDs

Chengdong Kong ⬤ https://orcid.org/0000-0003-3713-0653

References

[1] Gao J L, Kong C D, Zhu J J, Ehn A, Hurtig T, Tang Y, Chen S, Alden M and Li Z S 2019 Visualization of instantaneous structure and dynamics of large-scale turbulent flames stabilized by a gliding arc discharge *Proc. Combust. Inst.* **37** 5629–36

[2] Bak M S, Do H, Mungal M G and Cappelli M A 2012 Plasma-assisted stabilization of laminar premixed methane/air flames around the lean flammability limit *Combust. Flame* **159** 3128–37

[3] Ehn A, Zhu J J, Petersson P, Li Z S, Alden M, Fureby C, Hurtig T, Zettervall N, Larsson A and Larfeldt J 2015 Plasma assisted combustion: effects of O_3 on large scale turbulent combustion studied with laser diagnostics and large eddy simulations *Proc. Combust. Inst.* **35** 3487–95

[4] Kusano Y, Zhu J J, Ehn A, Li Z S, Alden M, Salewski M, Leipold F, Bardenshtein A and Krebs N 2015 Observation of gliding arc surface treatment *Surf. Eng.* **31** 282–8

[5] Wu C S, Wang L, Ren W J and Zhang X Y 2014 Plasma arc welding: process, sensing, control and modeling *J. Manuf. Process.* **16** 74–85

[6] Lin H F, Liao S C and Hung S W 2005 The dc thermal plasma synthesis of ZnO nanoparticles for visible-light photocatalyst *J. Photochem. Photobiol.* A **174** 82–7

[7] Mandal R, Singh A and Singh A P 2018 Recent developments in cold plasma decontamination technology in the food industry *Trends Food Sci. Technol.* **80** 93–103

[8] Zhu J J, Ehn A, Gao J L, Kong C D, Alden M, Salewski M, Leipold F, Kusano Y and Li Z S 2017 Translational, rotational, vibrational and electron temperatures of a gliding arc discharge *Opt. Express* **25** 20243–57

[9] Masoud N, Martus K, Figus M and Becker K 2005 Rotational and vibrational temperature measurements in a high-pressure cylindrical dielectric barrier discharge (C-DBD) *Contrib. Plasma Phys.* **45** 32–9

[10] Guedah H, Abahazem A, Merbahi N and Yousfi M 2017 Rotational, vibrational and electronic temperatures of pulsed corona discharge at atmospheric pressure in humid air *Rotational, Vibrational and Electronic Temperatures of Pulsed Corona Discharge at Atmospheric Pressure in Humid Air (Estoril/Lisbon, Portugal)*

[11] Roettgen A, Shkurenkov I, Simeni M S, Petrishchev V, Adamovich I V and Lempert W R 2016 Time-resolved electron density and electron temperature measurements in nanosecond pulse discharges in helium *Plasma Sources Sci. Technol.* **25** 055009

[12] Schaeffer D B *et al* 2012 Thomson scattering measurements of temperature and density in a low-density, laser-driven magnetized plasma *J. Instrum.* **7** P02002

[13] Xiong Q, Xu L, Wang X, Xiong L, Huang Q H, Chen Q, Wang J G, Peng W X and Li J R 2018 Full spatial-field visualization of gas temperature in an air micro-glow discharge by calibrated Schlieren photography *J. Phys. D: Appl. Phys.* **51** 095207

[14] Verreycken T, van Gessel A F H, Pageau A and Bruggeman P 2011 Validation of gas temperature measurements by OES in an atmospheric air glow discharge with water electrode using Rayleigh scattering *Plasma Sources Sci. Technol.* **20** 024002

[15] Lo A, Cessou A, Boubert P and Vervisch P 2014 Space and time analysis of the nanosecond scale discharges in atmospheric pressure air: I. Gas temperature and vibrational distribution function of N_2 and O_2 *J. Phys. D: Appl. Phys.* **47** 115201

[16] Brehmer F, Welzel S, Klarenaar B L M, van der Meiden H J, van de Sanden M C M and Engeln R 2015 Gas temperature in transient CO_2 plasma measured by Raman scattering *J. Phys. D: Appl. Phys.* **48** 155201

J. Phys. D: Appl. Phys. **53** (2020) 085502

C Kong *et al*

[17] Jiang N B, Hsu P S, Mance J G, Wu Y, Gragston M, Zhang Z L, Miller J D, Gord J R and Roy S 2017 High-speed 2D Raman imaging at elevated pressures *Opt. Lett.* **42** 3678–81

[18] Adams S F, Caplinger J E and Sommers B S 2015 Spatial temperature mapping of an atmospheric microdischarge using ultraviolet Rayleigh scatter imaging *Plasma Sources Sci. Technol.* **24** 025031

[19] Sommers B S and Adams S F 2015 A comparison of gas temperatures measured by ultraviolet laser scattering in atmospheric plasma sources *J. Phys. D: Appl. Phys.* **48** 485202

[20] Bruggeman P J, Sadeghi N, Schram D C and Linss V 2014 Gas temperature determination from rotational lines in non-equilibrium plasmas: a review *Plasma Sources Sci. Technol.* **23** 023001

[21] Prevosto L, Kelly H, Mancinelli B, Chamorro J C and Cejas E 2015 On the physical processes ruling an atmospheric pressure air glow discharge operating in an intermediate current regime *Phys. Plasmas* **22** 023504

[22] Zhu J J, Gao J L, Li Z S, Ehn A, Alden M, Larsson A and Kusano Y 2014 Sustained diffusive alternating current gliding arc discharge in atmospheric pressure air *Appl. Phys. Lett.* **105** 234102

[23] Sun Z W, Zhu J J, Li Z S, Alden M, Leipold F, Salewski M and Kusano Y 2013 Optical diagnostics of a gliding arc *Opt. Express* **21** 6028–44

[24] Ehn A, Zhu J, Li X and Kiefer J 2017 Advanced laser-based techniques for gas-phase diagnostics in combustion and aerospace engineering *Appl. Spectrosc.* **71** 341–66

[25] Popov N A 2016 Pulsed nanosecond discharge in air at high specific deposited energy: fast gas heating and active particle production *Plasma Sources Sci. Technol.* **25** 044003

[26] Popov N A 2006 Simulations of a longitudinal glow discharge in a hot air flow at atmospheric pressure *Plasma Phys. Rep.* **32** 237–45

[27] Sneep M and Ubachs W 2005 Direct measurement of the Rayleigh scattering cross section in various gases *J. Quant. Spectrosc. Radiat. Transfer* **92** 293–310

[28] Thalman R, Zarzana K J, Tolbert M A and Volkamer R 2014 Rayleigh scattering cross-section measurements of nitrogen, argon, oxygen and air *J. Quant. Spectrosc. Radiat. Transfer* **147** 171–7

[29] Tarafdar S P and Vardya M S 1969 Rayleigh scattering cross-sections of He, C, N and O *Mon. Not. R. Astron. Soc.* **145** 171–80

[30] Kong C D, Gao J L, Zhu J J, Ehn A, Alden M and Li Z S 2018 Re-igniting the afterglow plasma column of an AC powered gliding arc discharge in atmospheric-pressure air *Appl. Phys. Lett.* **112** 234102

[31] Gordon S and McBride J 1996 *Computer Program for Calculation of Complex Chemical Equilibrium Compositions and Applications. I Analysis* NASA Reference Publication 1311

[32] Richard F, Cormier J M, Pellerin S and Chapelle J 1996 Physical study of a gliding arc discharge *J. Appl. Phys.* **79** 2245–50

[33] Starikovskiy A and Aleksandrov N 2013 Plasma-assisted ignition and combustion *Prog. Energy Combust. Sci.* **39** 61–110

[34] Kong C D, Gao J L, Zhu J J, Ehn A, Alden M and Li Z S 2017 Characterization of an AC glow-type gliding arc discharge in atmospheric air with a current–voltage lumped model *Phys. Plasmas* **24** 013514

[35] Riousset J A, Pasko V P and Bourdon A 2010 Air-density-dependent model for analysis of air heating associated with streamers, leaders, and transient luminous events *J. Geophys. Res.* **115** A12321

[36] Prevosto L, Kelly H and Mancinelli B 2016 Modelling of an atmospheric pressure nitrogen glow discharge operating in high-gas temperature regimes *Plasma Chem. Plasma Process.* **36** 973–92